A Transition from Cylindrical to Spherical Morphology in Diblock Copolymer Thin Films

Ken-ichi Niihara,[†] Hidekazu Sugimori,[†] Ukyo Matsuwaki,[†] Fumio Hirato,[†] Hiroshi Morita,[‡] Masao Doi,[§] Hiroyasu Masunaga,[||] Sono Sasaki,[||] and Hiroshi Jinnai*[,†]

Department of Macromolecular Science and Engineering, Graduate School of Science and Engineering, Kyoto Institute of Technology, Matsugasaki, Kyoto 606-8585, Japan; Nanosimulation Research Group, Nanotechnology Research Institute, National Institute of Advanced Industrial Science and Technology, 1-1-1 Umezono, Tsukuba, Ibaraki 305-8568, Japan; Department of Applied Physics, The University of Tokyo, 7-3-1 Hongo, Bunkyo-ku, Tokyo 113-8656, Japan; and Japan Synchrotoron Radiation Research Institute, SPring-8, Kouto, Sayo-cho, Hyogo 679-5198, Japan

Received August 21, 2008; Revised Manuscript Received October 21, 2008

ABSTRACT: Microphase-separated structures in poly(styrene-*block*-isoprene) (SI) block copolymer thin films were investigated by transmission electron microtomography (TEMT). The SI block copolymer showed *cylindrical microdomains in the bulk state*. Several block copolymer thin films with different thicknesses were prepared by spin-coating and were extensively annealed before the TEMT experiments. Intriguingly, although the cylindrical morphology orienting parallel to the substrate was observed in most of the cases, *spherical microdomains* were found at certain film thicknesses. The thickness dependence was investigated using a computer simulation based on the self-consistent-field theory, producing a morphological phase diagram based on minimizing free energy. We find that the distortion of the hexagonal lattice of the cylindrical microdomains caused the morphological transition to the spherical microdomains.

1. Introduction

Block copolymers (BCPs) self-assemble into various types of highly periodic microphase-separated structures due to immiscibility between the dissimilar (A and B) sequences.[1,2] Microphase-separated structures of "block copolymer thin film(s)", which are confined inside a narrow space of the order of 10−100 nm, have been used in recent years in many technologies. These include microelectronic applications such as templates for nanopatterning, electrolyte films, and low-*k* films, as well as for nanoporous membranes.[3−10] The mechanical and electrical properties of those materials are believed to depend on the morphology, periodicity, orientation, and size of the microphase-separated structures. In order to understand BCP thin film morphologies and to develop these materials for industrial uses, it is particularly important to study in detail their self-assembly mechanisms.

The microphase-separated structures in BCP thin films are considerably affected by the surface interactions and the confinement. Two types of surface interactions are crucial: (i) between the BCP and the substrate and (ii) between the BCP and air. A number of studies have considered the effect of these interactions on the microphase-separated structures in BCP thin films using experiments[11−14] and computer simulations.[15−17]

Knoll et al. reported the phase behavior of BCP thin films using a cylinder-forming poly(styrene-*block*-butadiene-*block*-styrene) (SBS) triblock copolymers.[12−14,17,18] Surface morphologies of the SBS triblock copolymer thin films were examined by scanning force microscopy (SFM). A striped pattern, in which the SBS triblock formed cylinders aligned parallel to the film surface, was observed. Knoll et al. also observed a dotted SFM image in a thinner SBS thin film, which they regarded either the cylinders perpendicular to the film surface or a perforated layer (PL) structure. They also carried out computer simulations based on the dynamic density functional theory and dynamic self-consistent-field theory, which reproduced the observed morphological changes from the parallel cylinders to perpendicular cylinders (or PL). Although the morphologies obtained from the computer simulations also generated the perpendicular cylinders or the PL structure, it is still uncertain whether the SBS thin films actually had those morphologies because only two-dimensional (2D) topography at the exposed surface could be observed by SFM; the internal structures of the thin film were not investigated.

Transmission electron microtomography (TEMT), on the other hand, can provide internal as well as surface morphologies of the microphase-separated structures.[19,20] TEMT has been used in a considerable number of studies on microphase-separated structures, investigating, for example, the chain conformation inside microdomains,[21] morphologies,[22−26] grain boundary morphologies,[27,28] self-assembly processes,[29−31] and stability[32] of the microphase-separated structures.

In the present study, we examine the dependence of the microphase-separated structures of the cylinder-forming BCPs on film thickness using TEMT in order to obtain both in-plane and depth-dependent structural information in the BCP thin films. We also discuss the self-assembling mechanism of the microphase-separated structure formation in the BCP thin films using three-dimensional (3D) reconstructed images.

2. Experimental Section

A. Materials. Two poly(styrene-*block*-isoprene) (SI) BCPs were purchased from Polymer Source, Inc., Canada. The two BCPs are hereafter called SI_1 and SI_2. The number-average molecular weight (M_n) of the polystyrene (PS) and polyisoprene (PI) blocks in SI_1 are 40 800 and 10 400, respectively, and in SI_2 are 36 000 and 13 500, respectively. The polydispersity indexes (M_w/M_n) for both SI_1 and SI_2 are 1.06. The volume fractions of PI (ϕ_{PI}) in SI_1 and SI_2 are 0.23 and 0.35, respectively. The mass densities of PS and PI are 0.913 and 1.04 g/cm^3, respectively.[33]

B. Sample Preparation. In order to observe the bulk morphology of the SI BCPs, film specimens were prepared by casting from 5 wt % toluene solutions for ca. 10 days. The cast films were then

* To whom correspondence should be addressed: e-mail hjinnai@kit.ac.jp.
[†] Kyoto Institute of Technology.
[‡] National Institute of Advanced Industrial Science and Technology.
[§] The University of Tokyo.
[||] Japan Synchrotoron Radiation Research Institute.

10.1021/ma801892p CCC: $40.75
Published on Web 11/11/2008

Table 1. Thin Film Samples Used in the Experiments[a]

sample	code	concentration (wt %)	thickness[b] (nm)
SI_1	T1	2.2	87.1
SI_1	T2	2.4	100
SI_1	T3	2.6	113
SI_1	T4	3.0	135
SI_1	T5	3.4	150
SI_2	T6	2.0	87.3

[a] The concentration of the copolymer solution and film thickness of the spin-coated SI thin films are given. [b] The film thicknesses were measured from 3D images obtained by TEMT.

annealed at 120 °C for 1 day under vacuum. The annealed cast films were cut into a rod shape of ca. 0.5 mm cubic, in order to measure the small-angle X-ray scattering (SAXS), as detailed in the next section. The portion of the specimens used for the SAXS measurement was then ultramicrotomed using a diamond knife at −80 °C with a Lica Ultracut UCT. These ultrathin sections were transferred onto a Cu mesh grid with a polyvinylformal substrate.

The SI BCP thin films were prepared for TEMT analysis as follows. Mica substrates were cleaved and then coated with carbon by vacuum deposition. Five SI_1 thin films with different thicknesses were prepared by spin-coating from toluene solutions with five different concentration onto the mica substrates at 1700 rpm (see Table 1 for concentrations and thicknesses). An SI_2 thin film was of 87.3 nm thickness was also prepared by spin-coating from 2 wt % toluene solution onto the mica substrate at 1700 rpm. The film thicknesses were measured from 3D images obtained by TEMT. The thin films were annealed at 120 °C for 150 h under vacuum. The annealed thin films were then floated off the mica substrate using a water surface and were picked up onto Cu mesh grids for TEMT observations.

C. SAXS. SAXS measurement was carried out using the BL40B2 beamline at the Japan Synchrotron Radiation Research Institute (SPring-8, Hyogo, Japan). The wavelength, λ, was 0.15 nm. A focused X-ray beam of spot size 0.5 × 0.3 mm was used in the present study in order to measure the SAXS profile of a single grain of the microphase-separated structure. 2D scattering data were circularly averaged to obtain scattering profiles as a function of magnitude of the scattering vector, q ($q \equiv (4\pi/\lambda)\sin(\theta/2)$, where θ is the scattering angle).

D. TEM and TEMT. Prior to the observations with transmission electron microscopy (TEM) and TEMT, the ultrathin section and thin films were stained by OsO_4 vapor for 3 h. Gold particles (diameter = 10 nm) were then placed on the specimens using a gold colloidal solution (GCN005, BBInternational Co., Ltd., UK).

The TEM and TEMT experiments were carried out on a JEM-2200FS (JEOL Co., Ltd., Japan) operated at 200 kV and equipped with a slow-scan CCD camera (Gatan USC1000, Gatan Inc.) as the detector. Only the transmitted and elastically scattered electrons (electron energy loss of 0 ± 15 eV) were selected by the energy filter installed in the JEM-2200FS (Omega filter, JEOL Co., Ltd., Japan). TEM tilt series were taken through the range of angles from −60° to +60° with a 1° increment. They were then aligned by the fiducial marker method.[34] The mean alignment error,[35,36] averaged over all of the fiducial markers used in the alignment, was less than the 0.8 nm (where 1 pixel = 1.0 nm) regardless of the tilt angles. The tilt series after the alignment were subsequently reconstructed by the filtered back-projection algorithm.[37] All alignment and reconstruction procedures were carried out using software developed in our laboratory.

E. SCF Simulation. To investigate the stability of microphase-separated structures, the Helmholtz free energy of a system was calculated by a simulator called SUSHI in OCTA[38] based on self-consistent-field (SCF) theory.[39,40] In this theory, a polymer is modeled as a Gaussian chain that consists of N segments with Kuhn length, b. A polymer interacts with surrounding polymers in the system. This interaction is approximated as the mean field potential, $\mu(\mathbf{r})$. The $\mu(\mathbf{r})$ of a K segment, $\mu_K(\mathbf{r})$ (in present study, K is either PI or PS), is conjugate with the density, $\phi_K(\mathbf{r})$ ($\phi_K(\mathbf{r}) = 1 - \phi_{K'}(\mathbf{r})$), at the position $\mathbf{r}$ and the Flory−Huggins χ parameter according to the following equation:

$$\mu_K(\mathbf{r}) = \sum_{K'} \chi_{KK'}\phi_{K'}(\mathbf{r}) + \gamma(\mathbf{r}) \quad (1)$$

where $\gamma(\mathbf{r})$ is the constraint force due to external condition such as the incompressibility condition. The Helmholtz free energy per unit volume in the system consisting of segment K is given by

$$F(\phi_K, \mu_K) = -\frac{kT}{V}M \ln Z + \frac{1}{2V}\sum_{K,K'}\int \epsilon_{K,K}\phi_K(\mathbf{r})\phi_{K'}(\mathbf{r})\,d\mathbf{r} - \frac{1}{V}\sum_{K}\int \mu_K(\mathbf{r})\phi_K(\mathbf{r})\,d\mathbf{r} + \frac{kT}{V}M \ln M \quad (2)$$

where k, T, and V are the Boltzmann constant, absolute temperature, and calculated volume, respectively. M and Z are the number of polymer chain and the partition function, respectively. The first term of eq 2 corresponds to the conformational entropy of the chain. The second term is the interaction between segments. The third and fourth terms are the contribution from the constraint conditions and that from the mixing entropy, respectively. Each subscript indicates the component in the diblock copolymer. $\epsilon_{KK'}$ is the interaction energy between a pair of segments K and K' is related to $\chi_{KK'}$ by

$$\chi_{KK'} = \frac{z}{2kT}(\epsilon_{KK'} + \epsilon_{KK'} - \epsilon_{KK} - \epsilon_{K'K'}) \quad (3)$$

where z is the number of nearest-neighbor lattice sites. In the present study, the number of segments in the A−B (PS−PI) type diblock copolymers, N_A and N_B, are 117 and 33, respectively. The volume fraction of the B block (PI) is 0.23, and the $\chi_{AB}N$ is 24.0, which was estimated from a previous study[41] with same contents of diblock copolymer as the present study. Each parameter was compatible with experimental conditions.

3. Results and Discussion

A. Morphological Characterization in the Bulk State. Figure 1a shows a TEM micrograph of the SI_1 BCP in the bulk state. This copolymer self-assembled into a typical hexagonally packed cylindrical (HEX) morphology. The dark circles on the left-hand side of Figure 1a correspond to an "edge-on view", i.e., a view from the [001] direction of the HEX lattice, while the striped pattern on the right-hand side corresponds to the "side view", i.e., a view from the (100), (010), or (110) planes of the HEX lattice. Figure 1b shows a SAXS 2D diffraction pattern of the SI_1 BCP, which demonstrates distinct hexagonal diffraction spots arising from the HEX single grain. The 2D diffraction pattern was then circularly averaged (Figure 1c). The averaged SAXS profile of the SI_1 BCP exhibits multiple scattering maxima at peak positions $\sqrt{3}$, $\sqrt{4}$, and $\sqrt{7}$ relative to that of a first-order peak, as indicated by black arrows in Figure 1c. The SAXS results also demonstrated that the SI_1 BCP has the HEX morphology in the bulk state.[42,43] A schematic illustration of the edge-on cylinders is shown in the inset of Figure 1c. The interlayer distance, L_{cyl}, defined as the spacing between (100) planes of HEX, was evaluated to be 26.4 nm from $L_{cyl} = 2\pi/q_m$, where q_m is the wavenumber corresponding to the first-order peak in the SAXS profile. The interdomain distance, D_{cyl} ($= a = b$), defined as the spacing between (110) planes of HEX, was calculated to be 30.5 nm from $D_{cyl} = (4/3)^{1/2}L_{cyl}$, where γ is 120°. The diameter of a cylinder, $2R$, was estimated to be 15 nm from the TEM images. The structural parameters of the SI_1 BCP microdomain measured by SAXS were in good agreement with the parameters obtained from the TEM micrograph.

B. Dependence of Morphology on Thickness in BCP Thin Films. Figure 2 shows TEM micrographs of SI_1 BCP thin films of different thicknesses annealed at 120 °C for 150 h. In Figure 2, the Z-axis corresponds to the depth direction of the

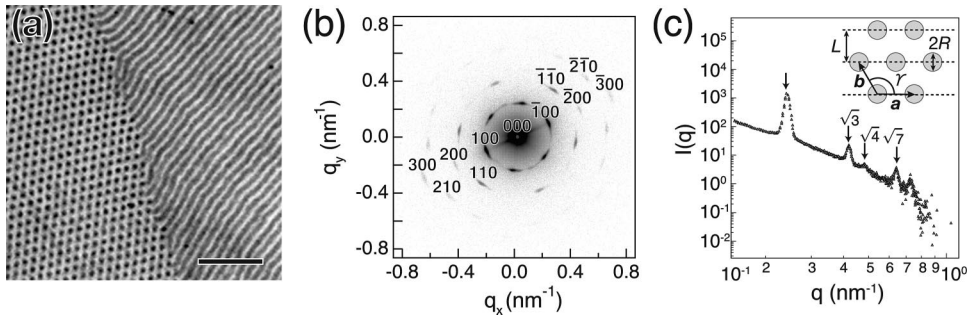

Figure 1. (a) TEM micrograph of an ultrathin section of SI_1 in the bulk, stained with OsO_4. The bright and dark phases correspond to PS and PI microdomains, respectively. The scale bar shows 200 nm. (b) 2D diffraction pattern of SI_1 in the bulk. Dark spots are the diffraction spots from the BCP microdomains. Each diffraction spot is labeled with the corresponding Miller index of the HEX lattice. (c) Circularly averaged SAXS profile. The inset in (c) shows a schematic illustration of the edge-on view of the HEX lattice. **a** and **b** are unit cell vectors, and γ is the angle between **a** and **b**. *L* corresponds to the interlayer distance of the cylindrical lattice: *L* represents the distance between (100) planes, and *R* corresponds to the radius of cylinder.

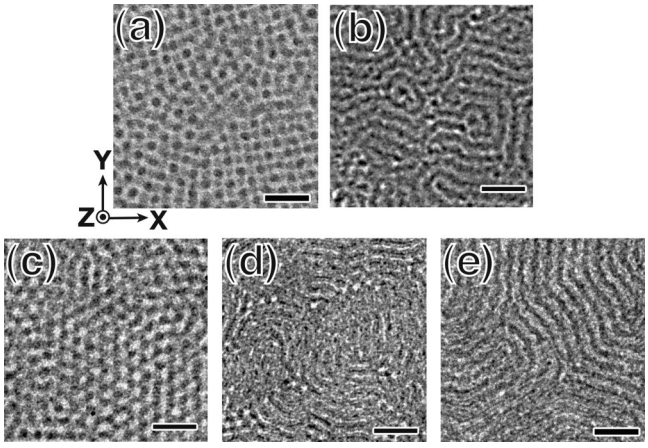

Figure 2. TEM micrographs of SI_1 thin films of different thicknesses stained with OsO_4 annealed at 120 ° C for 150 h. The films were spin-coated from (a) 2.2 wt % [film thickness 87 nm], (b) 2.4 wt % [100 nm], (c) 2.6 wt % [113 nm], (d) 3.0 wt % [135 nm], and (e) 3.4 wt % [150 nm]. Dark phase represents the stained PI microdomains. The *Z*-axis is along the depth of the thin film. Scale bars show 100 nm.

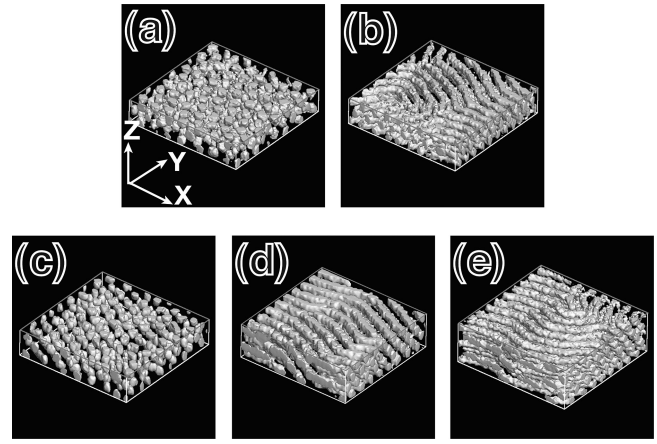

Figure 3. Surface rendered 3D images of SI_1 thin films stained with OsO_4 annealed at 120 °C for 150 h and spin-coated from (a) 2.2 wt % [film thickness 87 nm], (b) 2.4 wt % [100 nm], (c) 2.6 wt % [113 nm], (d) 3.0 wt % [135 nm], and (e) 3.4 wt % [150 nm]. White phase is the PI microdomains, while the PS microdomain is transparent. The edges of the 3D images along the *X*- and *Y*-axes are common for all volumed data and are 300 nm in length. The edge along the *Z*-axis varies according to the film thickness.

SI_1 BCP thin films. Two distinct patterns, stripelike and dotlike, were observed. Figures 2b,d,e appear to be stripelike, while Figures 2a,c are dotlike. The former, the stripe pattern, may arise from the cylinders ordering parallel to the substrate surface. It is commonly believed that the cylinders tend to align parallel to the substrate surface due to the preference of one of the blocks for the substrate surface (or the air surface).[44−46] The dotlike pattern likely arises from "edge-on cylinders", i.e., the cylinders oriented parallel to the *Z*-axis, or even the PL morphology as reported in previous studies.[12−14,17] Thus, the 3D morphologies inside the SI_1 thin films apparently depend on the film thickness.

The annealed thin films were tilted in the TEM to take a series of TEM projections to produce a 3D reconstruction. The tilt axis is parallel to the *Y*-axis (see Figure 2). The resulting reconstructed 3D images of the SI_1 thin films are shown in Figure 3. The 3D images were then digitally sliced in three different planes in order to examine the internal structures in more detail by eliminating the overlap of the microdomains. Figure 4 shows these orthogonal cross-sectional views of the 3D reconstructed data of the T3 thin film (113 nm). The PI microdomains of T3 show circular morphology in the three orthogonal planes. Although not shown here, exactly the same morphological features were observed in the T1 thin film (87 nm). The 3D images make clear that the T1 and T3 thin films, surprisingly, exhibited three-layered PI *spherical microdomains* in the PS matrix. We emphasize here that the equilibrium structure of this copolymer *in the bulk state* is the cylindrical morphology. On the other hand, the T2, T4, and T5 thin films exhibited cylindrical microdomains parallel to the substrate surface. These were three-, four-, and five-layered cylindrical microdomains, respectively. Note that all the SI_1 BCP thin films had wetting PI layers both at the substrate and at the air surfaces due to the smaller surface tension of PI compared to that of PS. The PI wetting layers were confirmed by a separate cross-sectional TEM experiment (not shown here).[29,47] The wetting layers, however, cannot be reconstructed due to the insufficient tilt angular range of our experiment geometry.[45] The positions of the air and substrate surfaces in the 3D images were determined by the gold particles and/or small dust particles attached to these surfaces (shown in the $X-Z$ sliced image in Figure 4). The (averaged) film thicknesses of the thin films, *T*, were measured from the 3D images and are listed in Table 1. Note that the thicknesses of the BCP thin films were rather uniform for all specimens.

C. Characterization of the Spherical Lattice. In this section, we characterize the spherical lattice observed in the SI_1 BCP thin films T1 and T3. Figure 4 shows a 3D orthogonal image of the T3 film. The spatial arrangement of the PI spherical microdomains is clearly defined in the sliced images. The PI spheres are arranged in a hexagonally packed lattice in the $X-Y$ plane that is parallel to the substrate surface. The body-centered cubic (BCC), face-centered cubic (FCC), and hexagonal close-

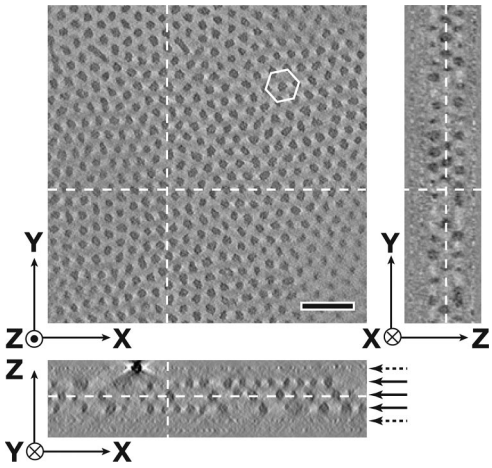

Figure 4. Orthogonal views of the T3 thin film annealed at 120 °C for 150 h. Dark and bright phases show the PI and PS microdomains, respectively. The *Z*-axis corresponds to the depth direction of the film. Dashed lines in each cross section represent the position of the other two orthogonal cross sections. Solid arrows in the $X-Z$ plane indicate three layers of the PI spherical microdomains. Dashed arrows indicate the positions of the free surface (top) and substrate surface (bottom). Scale bar is 100 nm.

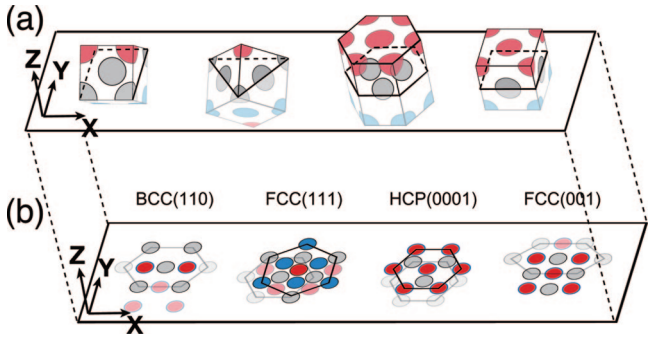

Figure 5. (a) Schematic illustration of the bird's-eye view of the four kinds of lattices that exhibit the hexagonal pattern observed in the $X-Y$ plane. The color of the spheres indicates the spheres in the three consecutive $X-Y$ slices. (b) The projected images of part (a).

packed (HCP) lattices show such hexagonal patterns at certain crystallographic planes. Figure 5 illustrates four possible lattice geometries. In Figure 5a, the gray spherical domains are located on an $X-Y$ plane in the 3D reconstructed data from the $X-Y$ digital slice in Figure 4, and the red and blue spheres are out of the $X-Y$ plane. Projected images of the gray spheres are shown in Figure 5b, in which the solid and translucent spheres belong to the lattices in Figure 5a and to the adjacent lattice. Thus, the gray spheres form a hexagonal pattern in the $X-Y$ digital slice as illustrated in Figure 5b. Although the FCC(001) plane in our sample shows somewhat skewed hexagonal pattern, we nonetheless include this possibility because the experimental hexagonal patterns in the digital slices are not always perfectly hexagonal. As shown in Figure 5b, the positions of the spherical domains in the adjacent three $X-Y$ layers are different depending on the lattice type and the crystallographic planes of the spherical lattices. For example, in the case of FCC(111) plane, the positions of the spherical domains in the adjacent three crystal planes do not overlap. On the other hand, as seen in Figure 5b, the red and blue circles belonging to adjacent upper and lower crystal planes in the other three cases do overlap. To identify which of the three possible lattice types is the correct one, we consider the relative positions of the red and blue circles with respect to the gray ones.

Three consecutive $X-Y$ digital slices of the T3 thin film were chosen. They were first binarized in order to find the interface

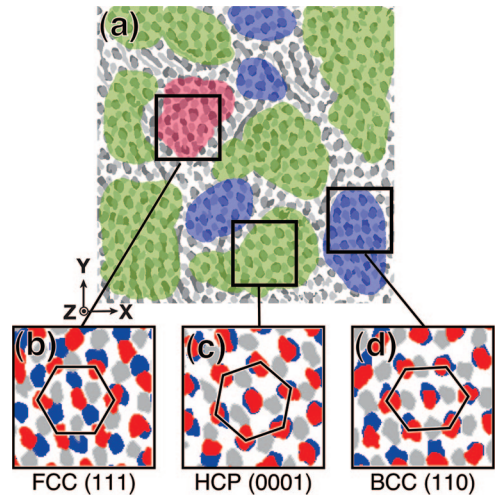

Figure 6. (a) Overlapped $X-Y$ sliced image of the T3 thin film annealed at 120 °C for 150 h. The colored regions of green, red, and blue correspond to the spherical microdomains formed HCP, FCC, and BCC lattices, respectively. Parts b–d are expanded images corresponding to the rectangles in (a). The color of the spheres indicates the spheres in the three consecutive the $X-Y$ slice.

between the spherical PI domains and the PS matrix. Subsequently, as shown in Figure 6a, the slices were overlapped to differentiate FCC(111) from other three types. Parts b, c, and d of Figure 6 show enlarged overlapped spherical domains corresponding to FCC(111), HCP(0001), and BCC(110), respectively. Clearly, the spherical domains in the three layers did not overlap in Figure 6b, while the red and blue spheres largely overlapped (although the gray spheres are in different locations) in the other two cases. This analysis leads us to conclude that the HCP lattice with the (0001) crystallographic plane being parallel to the substrate was found to be dominant, while a small fraction of BCC and FCC lattices were also found in the T3 thin films. Note that the analysis was carried out over a wider area than that shown in Figure 6a.

The spherical lattice of the T1 thin film was identified in the same manner. We found T1 to consist primarily of the FCC lattice with the (001) plane being parallel to the substrate, while the BCC lattice was minor. In contrast, the T2, T4, and T5 films, as discussed, consisted of three-, four-, and five-layered cylinders parallel to the substrate, respectively. These cylinders were hexagonally packed but curved in the $X-Y$ plane parallel to the substrate. We note here that the thin films thicker than T5 (thickness ca. 150 nm) never exhibited a spherical morphology.

It is well-known that sphere-forming BCPs normally self-assemble to form a BCC lattice in the bulk.[43] Our BCP thin films, in contrast, formed either HCP or FCC spheres. To investigate the physics behind this surprising phenomenon, we examined the structural formation process of the T3 BCP thin film during the thermal annealing as detailed in the next section.

D. Process of the Morphological Transition in the Thin Film. Figure 7 shows 3D images of the T3 thin film after three different annealing times, 0, 48, and 150 h. The microphase-separated structure right after the spin-casting (as-spun film) showed "bicontinuous-like" morphology,[29,48] in which the PI microdomains were continuous not only in the lateral $X-Y$ direction but also in the *Z* depth direction (see Figure 7a). After 48 h of annealing, this bicontinuous-like morphology changed to a cylinder-like morphology parallel to the substrate (Figure 7b). The cylindrical microdomains did not form a hexagonally packed lattice as they do in the bulk state. After 150 h of annealing, the T3 thin film formed HCP spheres (Figure 7c). The morphology did not change upon further annealing. The

Figure 7. Surface rendered 3D images of the T3 thin films after annealing at 120 °C for (a) 0, (b) 48, and (c) 150 h. White phase is the PI microdomains, while the PS microdomain is transparent. The edges of the 3D images along the *X*- and *Y*-axes are common for all volumed data and are 300 nm in length. The edge along the *Z*-axis is the film thickness, ca. 110 nm.

film thickness of ~110 nm did not change throughout the annealing process. The existence of wetting PI layers was confirmed by a separate cross-sectional TEM observation (not shown here). The thin films annealed for 48 and 150 h contained wetting PI layers both at the substrate surface and at the air surface. The existence of the wetting layers before the morphological transition from cylinders into spheres suggests that the wetting layers may not be the cause of the transition. Another indication that the morphological transition may not be arisen by the surface interactions is the fact that the PI layers closest to the wetting PI layers in the T2, T4, and T5 thin films never displayed spherical morphology. If the surface interaction played a substantial role in the morphological transition, the cylindrical layers closest to the wetting PI layers should exhibit spherical morphology in all the BCP thin films.

In order to understand the mechanism of the morphological transition, it is important to examine the evolution of the BCP morphology through the transition from cylinders into spheres.[43] A closeup $X-Y$ digital sliced image of the T3 film annealed at 120 °C for 150 h is shown in Figure 8. Inside the spherical domains, short cylindrical domains were observed, which are likely the "trace" of the cylinders before the morphological transition. The direction of the transition (from the cylinders into the spheres) was estimated from this trace. Figure 9a is a schematic showing how the cylinders can change into HCP spheres in the T3 film. The cylinders break up into multiple spheres. Thus, the [001] direction of the HEX should be the $[\bar{1}\bar{1}20]$ direction of the HCP spherical microdomains. From this relationship, the cylindrical lattice constant just before the transition can be estimated by measuring the spherical lattice constant. As illustrated in Figure 9a, the interdomain distance of the cylindrical microdomains, D_{cyl}, just before the transition into HCP spherical microdomains is related to the interdomain distance of the spherical microdomains, D_{sph}, as $D_{cyl} = (3/4)^{1/2}D_{sph}$. The analogous transitions into BCC and FCC spherical microdomains are shown in parts b and c of Figure 9, respectively. In these case the [001] direction of the HEX transformed into the [001] direction of the BCC and the [110] direction of the FCC spherical microdomains. Therefore, the BCC lattice follows the relation $D_{cyl} = (8/9)^{1/2}D_{sph}$, while the FCC lattice follows the relation $D_{cyl} = D_{sph}$ (Figures 9b,c). The interlayer distances of the cylindrical microdomains (L_{cyl}) are identical with the interlayer distances of the spherical microdomains (L_{sph}). Thus, D_{cyl} and L_{cyl} of the cylindrical lattice in the T3 thin film just before the transition from the HEX into the HCP (Figure 9a) were evaluated to be approximately 30.4 and 28.8 nm, respectively. Note that D_{cyl} and L_{cyl} *in the bulk state* are 30.5 and 26.4 nm, respectively (see section 3.A]. We suggest, therefore, that the cylindrical microdomains of the T3 thin film just before the transition into the HCP spheres become somewhat distorted; i.e., L_{cyl} was larger than that of the bulk by 9%. Similarly, the cylindrical morphology of the T1 thin film just before the transition into FCC spherical morphology

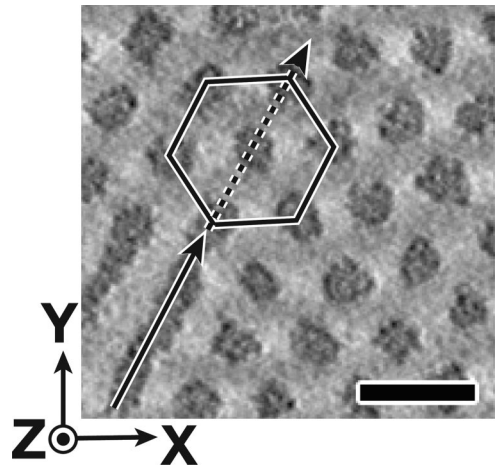

Figure 8. A close-up view of the $X-Y$ sliced image of the T3 thin film annealed at 120 °C for 150 h. Dark and bright phases are the PI and PS microdomains, respectively. The solid arrow indicates the cylinder [001] direction, and the dashed arrow indicates the HCP $[\bar{1}\bar{1}20]$ direction. Scale bar is 50 nm.

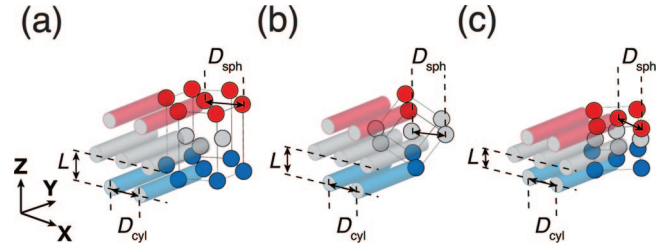

Figure 9. Schematic illustrations showing the transition from cylindrical microdomains into spherical microdomains. Parts a, b, and c correspond to the transitions from the cylindrical microdomains into the HCP, BCC, and FCC spherical microdomains, respectively. The *Y*-direction corresponds to the cylinder [001] direction. *L* and *D* are the interlayer distance and interdomain distance, respectively.

was also distorted: L_{cyl} was 20% smaller than that of the bulk, while D_{cyl} was larger than that of the bulk by 10%.

In a related study, Knoll et al.[46] investigated the distortion of the cylindrical lattice in a poly(styrene-*b*-butadiene) BCP thin film using SFM. They found that the HEX lattice became distorted when the film thickness, *T*, did not fulfill the condition $T = mL$, where m is an integer. In our case, the cylindrical lattice just before the transition in the T1 and T3 thin films also did not meet this condition and therefore became distorted. Knoll et al. also demonstrated that the degree of distortion decreased as the number of the cylindrical layers increased.[46] Our results are consistent with this finding, as no morphological transition was observed in any of the SI_1 BCP thin films thicker than T3, probably due to the smaller distortion of the cylindrical lattice.

Thus far we have examined the morphological transition from the cylindrical into spherical microdomains as a result of the cylindrical lattice becoming distorted before the transition. We now consider whether the PI volume fraction, ϕ_{PI}, plays an important role in this transition. The SI_1 BCP used in the above experiments has ϕ_{PI} equal to 0.23, which is close to the edge between the spheres and cylinders in the phase diagram.[49] We therefore chose the BCP SI_2, with a ϕ_{PI} of 0.35, to further study the morphological transition. Note that $\phi_{PI} = 0.35$ is almost at the border between the cylindrical phase and the gyroid phase.[49] As expected, SI_2 showed the HEX morphology in the bulk state (not shown here). Parts a and b of Figure 10 show a TEM micrograph and a 3D image, respectively, of the T6 thin film. The TEM micrograph of the T6 thin film after annealing at 120 °C for 150 h (Figure 10a) shows a dotted pattern similar to the

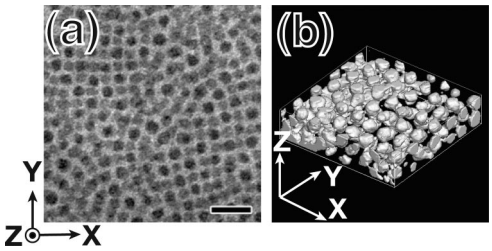

Figure 10. (a) A TEM micrograph and (b) a surface rendered 3D image of the T6 thin film stained with OsO_4 annealed at 120 °C for 150 h. In (a), the dark and bright phases correspond to the PI and PS microdomains, respectively. Scale bar is 100 nm. In (b), white phase is the PI microdomains, while the PS microdomain is transparent. The edges of the 3D images along the *X*- and *Y*-axes are common for all volumed data and are 300 nm in length. The edge along the *Z*-axis is the film thickness, ca. 87 nm.

T1 and T3 thin film (see Figures 2a,c). The film thickness was 87.3 nm, which was measured from the 3D image. The T6 thin film also showed three-layerd PI spheres in an FCC lattice in the PS matrix (see Figure 10b). The cylindrical microdomain just before the transition into spherical microdomain in the T6 thin film was also distorted; L_{cyl} was smaller by 20% than that of the bulk, while D_{cyl} was 15% larger than that of the bulk. This result suggests that the morphological transition occurs irrespective of the position of ϕ_{PI} on the phase diagram. Note that the PI volume fractions in the T1, T3, and T6 evaluated from the 3D images were close to the corresponding bulk volume fractions.

E. Mechanism of the Morphological Transition. Stein et al. investigated the thickness dependence of sphere-forming BCP thin films using GISAXS, TEM, and SCF simulation.[50,51] They found that the spherical microdomains transitioned from a BCC lattice into different types of spherical lattice at certain film thickness due to the distortion of the spherical lattice. In our case, the morphological transition may be caused by the increase in free energy due to the distortion of the cylindrical morphology, although the transition in this case is more drastic than that in Stein's case.

Matsen et al. discussed the stability of the distorted cylindrical morphology in diblock copolymers.[39,52] They calculated the free energy of the cylindrical phase parallel to the substrate as a function of the aspect ratio of the cylindrical lattice using a computer simulation based on the strong segregation and the SCF theories. In the present study, the Helmholtz free energy of the cylindrical morphology was calculated as a function of D_{cyl} and L_{cyl} using an SCF simulation in order to investigate the stability of the cylindrical structure.

First, the mesh size of the simulation was decided on the basis of any given combination of D_{cyl} and L_{cyl}. Second, we used SCF simulation to calculate the densities of the *K* block chain (*K* is either PI or PS) and the mean field potential, $\mu_K(\mathbf{r})$, at any given position, $\mathbf{r}$, of the cylindrical structure with each of the hexagonal symmetries. Subsequently, the free energy per unit volume, $F(\phi_K, \mu_K)$, was calculated from eq 2. Note that the SCF simulation did not consider interactions between the BCP and substrate and between the BCP and air. This choice was justified because the contribution of the surface interaction to the morphological transition appears to be very small in our system, as described in section 3.D.

Figure 11a shows the calculated free energy diagram of the cylindrical microdomains as a function of D_{cyl} and L_{cyl}. The free energy of the HEX morphology in the bulk state is indicated by a cross, representing the minimum free energy value, as expected. Note that D_{cyl} and L_{cyl} of the bulk state were determined from experimental results. The free energy of the

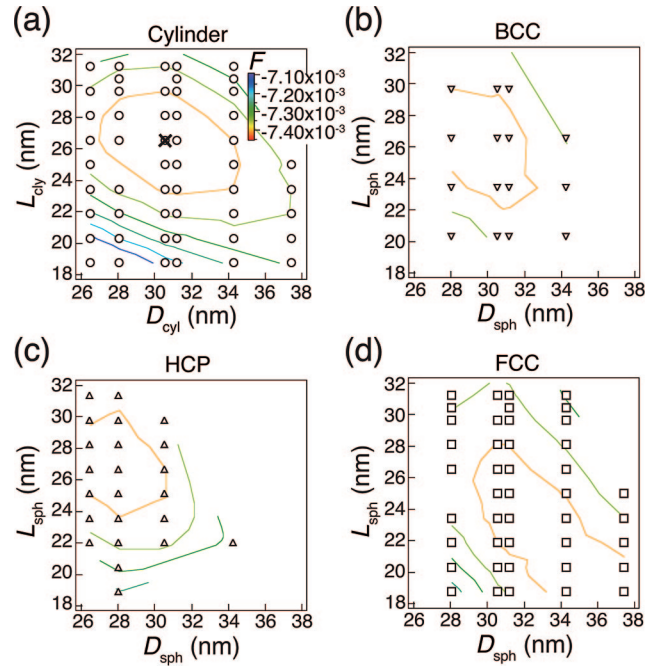

Figure 11. Free energy diagrams as functions of *L* and *D* for the studied morphologies as calculated by SCF simulation: (a) cylinder, (b) BCC, (c) HCP, and (d) FCC. Open symbols are calculated points. The cross in (a) indicates the location of *L* and *D* in the bulk state. Colored solid lines are the contour lines of the free energy.

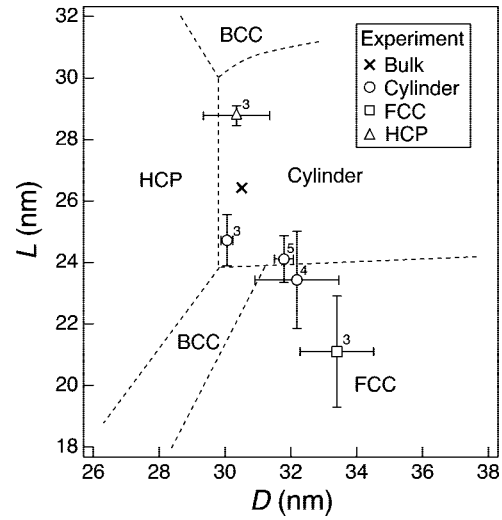

Figure 12. Morphological "phase diagram" showing the stable morphologis as a function of *L* and *D*, evaluated from the free energy diagrams shown in Figure 11. Dashed lines are the boundaries between different morphologies. The open symbols are experimentally obtained values from 3D images. The cross indicates the location of *L* and *D* in the bulk state.

cylindrical morphology became higher as D_{cyl} and L_{cyl} deviated from the bulk values.

The free energies of the BCC, FCC, and HCP spherical morphologies with the same range of D_{cyl} and L_{cyl} as those in Figure 11a were also calculated in the same way. The calculated free energy diagrams of the BCC, FCC, and HCP spherical morphologies are shown in parts b, c, and d of Figure 11, respectively.

The most stable morphology in the thin film was decided from the energy maps of Figure 11. Specifically, the morphology that has the lowest free energy at the D_{sph} (or D_{cyl}) and L_{sph} (or L_{cyl}) is considered to be the most stable. The stability diagram

based on this evaluation is shown in Figure 12. On this "phase diagram", D and L corresponding to the T1 to T5 thin films (measured from 3D images) are also plotted. The experimental results agree reasonably well with the SCF prediction of which lattice type will be the most stable for each film, considering that the resolution of our TEMT is ca. 1 nm.[53] Within the experimental error (shown in Figure 12), the trend is clear. We therefore conclude that the morphological transition observed in this study is due to the destabilization of the distorted HEX microdomains.

We here note that multiple types of spherical lattices have been found in T1 and T3 thin film. For example, although the HCP lattice is stable according to the phase diagram shown in Figure 12 and thus dominant in the T3 thin film, the BCC and FCC lattices were also found (see Figure 6a). We speculate that the origin of the coexistence of the BCC and FCC lattices in the T3 thin film is kinetic. As demonstrated in Figure 7b, although the cylindrical microdomains are parallel to the substrate, they are not perfectly aligned but curved in the lateral plane, i.e., $X-Y$ plane. Thus, when the breakup of the cylindrical microdomains to the spherical ones took place during the morphological transition, the resulting spherical generated from such curved cylinders turned to energetically unfavorable types of lattices, i.e., BCC and FCC lattices. If the higher alignment of the HEX morphology before the morphological transition could be achieved using a similar protocol in the literature,[54,55] such coexistence of the unfavorable lattices would be avoided.

4. Conclusions

A morphological transition of a *cylinder-forming* poly(styrene-*block*-isoprene) (SI) thin film was studied by transmission electron microtomography (TEMT) and by a self-consistent-field (SCF) computer simulation. Unexpectedly, a spherical morphology was observed in a few SI thin films. The thicknesses of the films with spherical structure were not integer multiples of the interlayer distance in the cylindrical morphology. The annealing process of the sphere-forming thin films was investigated by TEMT. Upon annealing, the morphology changed from an as-spun thin film forming a bicontinuous-like morphology into cylindrical morphology and then further into hexagonal close-packed (HCP) or face-centered cubic (FCC) spherical morphologies. The lattice parameters of the cylindrical microdomains just before the morphological transition from cylinders into spheres were determined from the trace of the cylinders in the spherical microdomains. The cylindrical lattice was found to be distorted from the bulk state lattice. The free energy of the distorted cylindrical structures and the spherical structures were calculated by a computer simulation based on the SCF theory. The free energy of the distorted cylindrical morphology just before the transition was higher than that of the spherical lattice. Thus, the distorted cylindrical morphology transformed into spherical morphologies in order to decrease the free energy. The stable spherical lattice after the transition depends on the degree of distortion. In addition, films thicker than T5 did not form spheres because the free energy associated with the distortion of the cylindrical lattice was negligibly small to cause the morphological transition.

Acknowledgment. The authors are grateful to NEDO for supporting this study through a Japanese National Project "Nano Structured Polymer Project" by the Ministry of Economy, Trade and Industry. This work is partially supported by the Ministry of Education, Science, Sports and Culture through Grant-in-Aid and No. 19031016. The authors are grateful to Prof. K. Tanaka of Kyushu University for his valuable discussion and comments. The authors also thank Mr. K. Matsunaga of the Department of Macromolecular Science and Engineering, Kyoto Institute of Technology, for his contribution of the TEMT experiments.

Supporting Information Available: Movies of T2 and T3 thin films. This material is available free of charge via the Internet at http://pubs.acs.org.

References and Notes

(1) Hamley, I. W., Ed.; *Developments in Block Copolymer Science and Technology*; John Wiley & Sons Ltd.: New York, 2004.
(2) Abetz, V.; Simon, P. F. W. Block Copolymers I. In *Advances in Polymer Science*; Abetz, V., Ed.; Springer: Berlin, 2005.
(3) Guarini, K. W.; Black, C. T.; Zhang, Y.; Kim, H.; Sikorski, E. M.; Babich, I. V. *J. Vac. Sci. Technol. B* **2002**, *20*, 2788–2792.
(4) Hamley, I. W. *Nanotechnology* **2003**, *14*, R39−R54.
(5) Stoykovich, M. P.; Muller, M.; Kim, S.; Solak, H. H.; Edwards, E. W.; Pablo, J. J.; Nealey, P. F. *Science* **2005**, *308*, 1442–1446.
(6) Widawski, G.; Rawiso, M.; François, B. *Nature (London)* **1994**, *369*, 387–389.
(7) Freer, E. M.; Krupp, L. E.; Hinsberg, W. D.; Rice, P. M.; Hedrick, J. L.; Cha, J. N.; Miller, R. D.; Kim, H. *Nano Lett.* **2005**, *5*, 2014–2018.
(8) Peinemann, K.; Abetz, V.; Simon, P. W. *Nat. Mater.* **2007**, *6*, 992–996.
(9) Li, J.; Kamata, K.; Komura, M.; Yamada, T.; Yoshida, H.; Iyoda, T. *Macromolecules* **2007**, *40*, 8125–8128.
(10) Ro, H. W.; Peng, H.; Niihara, K.; Lee, H.; Lin, E. K.; Karim, A.; Gidley, D. W.; Jinnai, H.; Yoon, D. Y.; Soles, C. L. *Adv. Mater.* **2008**, *20*, 1934–1939.
(11) Fasolka, M. J.; Mayes, A. M. *Annu. Rev. Mater.* **2001**, *31*, 323–355.
(12) Knoll, A.; Horvat, A.; Lyakhova, K. S.; Krausch, G.; Sevink, G. J. A.; Zvelindovsky, A. V.; Magerle, R. *Phys. Rev. Lett.* **2002**, *89*, 035501.
(13) Knoll, A.; Magerle, R.; Krausch, G. *J. Chem. Phys.* **2004**, *120*, 1105–1116.
(14) Tsarkova, L.; Knoll, A.; Krauschand, G.; Magerle, R. *Macromolecules* **2006**, *39*, 3608–3615.
(15) Huinink, H. P.; van Dijk, M. A.; Brokken-Zijp, J. C. M.; Sevink, G. J. A. *Macromolecules* **2001**, *34*, 5325–5330.
(16) Wang, Q.; Nealey, P. F.; de Pablo, J. J. *Macromolecules* **2001**, *34*, 3458–3470.
(17) Horvat, A.; Lyakhova, K. S.; Sevink, G. J. A.; Zvelindovsky, A. V.; Magerie, R. *J. Chem. Phys.* **2004**, *120*, 1117–1126.
(18) Horvat, A.; Knoll, A.; Krausch, G.; Tsarkova, L.; Lyakhowa, K.; Sevink, G. J. A.; Zvelindovsky, A. V.; Magerle, R. *Macromolecules* **2007**, *40*, 6930–6939.
(19) Frank, J. Principles of Electron Tomography. In *Electron Tomography*; Frank, J., Ed.; Plenum Press: New York, 1992.
(20) Jinnai, H.; Ikehara, T.; Nishi, T. *Adv. Polym. Sci.* **2004**, *170*, 115–167.
(21) Morita, H.; Kawakatsu, T.; Doi, M.; Nishi, T.; Jinnai, H. *Macromolecules* **2008**, *41*, 4845–4849.
(22) Spontak, R. J.; Williams, M. C.; Agard, D. A. *Polymer* **1988**, *29*, 387–395.
(23) Radzilowsk, L. H.; Crragher, B. O.; Stupp, S. I. *Macromolecules* **1997**, *30*, 2110–2119.
(24) Yamauchi, K.; Takahashi, K.; Hasegawa, H.; Iatrou, H.; Hadjichristidis, N.; Kaneko, T.; Nishikawa, Y.; Jinnai, H.; Matsui, T.; Nishioka, H.; Shimizu, M.; Furukawa, H. *Macromolecules* **2003**, *36*, 6962–6966.
(25) Kaneko, T.; Suda, K.; Satoh, K.; Kamigaito, M.; Kato, T.; Ono, T.; Nakamura, E.; Nishi, T.; Jinnai, H. *Macromol. Symp.* **2006**, *242*, 80–86.
(26) Niihara, K.; Matsuwaki, U.; Torikai, N.; Atarashi, H.; Tanaka, K.; Jinnai, H. *Macromolecules* **2007**, *40*, 6940–6946.
(27) Jinnai, H.; Sawa, K.; Nishi, T. *Macromolecules* **2006**, *39*, 5815–5819.
(28) Jinnai, H.; Yasuda, K.; Nishi, T. *Macromol. Symp.* **2006**, *245* (246), 170–174.
(29) Niihara, K.; Nishikawa, Y.; Nishi, T.; Jinnai, H. *Trans. Mater. Res. Soc. Jpn.* **2005**, *30*, 617–622.
(30) Xu, T.; Zvelindovsky, A. V.; Sevink, G. J. A.; Lyakhova, K. S.; Jinnai, H.; Russell, T. P. *Macromolecules* **2005**, *38*, 10788–10798.
(31) Dohi, H.; Kimura, H.; Kotani, M.; Takeshi, K.; Kitaoka, T.; Nishi, T.; Jinnai, H. *Polym. J.* **2007**, *39*, 749–758.
(32) Jinnai, H.; Nishikawa, Y.; Spontak, R. J.; Smith, S. D.; Agard, D. A.; Hashimoto, T. *Phys. Rev. Lett.* **2000**, *84*, 518–521.
(33) Brandrup, J., Immergut, E. H., Grulke, E. A., Eds.; *Polymer Handbook*; John Wiley & Sons Ltd.: New York, 1999.
(34) Lawrence, M. C. *Macromolecules* **1997**, *30*, 2110–2119.
(35) Spontak, R. J.; Fung, J. C.; Braunfeld, M. B.; Sedat, J. W.; Agard, D. A.; Kane, L.; Smith, S. D.; Satkowski, M. M.; Ashraf, A.; Hadjuk, D. A.; Gruner, S. M. *Macromolecules* **1996**, *29*, 4494–4507.
(36) Kaneko, T.; Nishioka, H.; Nishi, T.; Jinnai, H. *J. Electron Microsc.* **2005**, *54*, 437–444.
(37) Crowther, R. A.; DeRosier, D. J.; Klug, A. *Proc. R. Soc. London* **1970**, *A 317*, 319–340.
(38) OCTA, http://octa.jp/.

(39) Matsen, M. W. *Phys. Rev. E* **2003**, *67*, 023801.
(40) Matsen, M. W.; Schick, M. *Phys. Rev. Lett.* **1994**, *72*, 2660–2663.
(41) Morita, H.; Kawakatsu, T.; Doi, M.; Yamaguchi, D.; Takenaka, M.; Hashimoto, T. *Macromolecules* **2002**, *35*, 7473–7480.
(42) Hajduk, D. A.; Gruner, S. M.; Rangarajan, P.; Register, R. A.; Fetters, L. J.; Honeker, C.; Albalak, R. J.; Thomas, E. L. *Macromolecules* **1994**, *27*, 490–501.
(43) Kimishima, K.; Koga, T.; Hashimoto, T. *Macromolecules* **2000**, *33*, 968–977.
(44) Karim, A.; Guo, L.; Rafailovichi, M. H.; Sokolov, J.; Peiffer, D. G.; Schwarz, S. A.; Colby, R. H.; Dozier, W. D. *J. Chem. Phys.* **1994**, *100*, 1620–1629.
(45) Sugimori, H.; Nishi, T.; Jinnai, H. *Macromolecules* **2005**, *38*, 10226–10233.
(46) Knoll, A.; Tsarkova, L.; Krausch, G. *Nano Lett.* **2007**, *7*, 843–846.
(47) Hasegawa, H.; Hashimoto, T. *Macromolecules* **1985**, *18*, 589–590.
(48) Fukunaga, K.; Hashimoto, T.; Elbs, H.; Krausch, G. *Macromolecules* **2002**, *35*, 4406–4413.
(49) Khandpur, A. K.; Forster, S.; Bates, F.; Hamley, I. W.; Ryan, A. J.; Bras, W.; Almdal, K.; Mortensen, K. *Macromolecules* **1995**, *28*, 8796–8806.
(50) Stein, G. E.; Kramer, E. J.; Li, X.; Wang, J. *Macromolecules* **2007**, *40*, 2453–2460.
(51) Stein, G. E.; Cochran, E. W.; Katsov, K.; Fredrikson, G. H.; Kramer, E. J.; Li, X.; Wang, J. *Macromolecules* **2007**, *40*, 2453–2460.
(52) Pereira, G. G. *Phys. Rev. E* **2001**, *63*, 061809.
(53) Nishiokai, H.; Niihara, K.; Kaneko, T.; J.; Yamanaka, Y. N. T. I.; Nishi, T.; Jinnai, H. *Ultramicroscopy* **2007**, *107*, 8–15.
(54) Lee, B.; Park, I.; Yoon, J.; Park, S.; Kim, J.; Kim, K.; Chang, T.; Ree, M. *Macromolecules* **2005**, *38*, 4311–4323.
(55) Berry, B. C.; Bosse, A. W.; Douglas, J. F.; Jones, R. L.; Karim, A. *Nano Lett.* **2007**, *7*, 2789–2794.

MA801892P